Eur. Phys. J. Spec. Top. (2022) 231:4233–4244
https://doi.org/10.1140/epjs/s11734-022-00571-0

THE EUROPEAN PHYSICAL JOURNAL SPECIAL TOPICS

Regular Article

Co, Fe and CoFe oxide nanoparticle assemblies within an ordered silica matrix: effects of the metal ions and synthesis pathway on the microstructure and magnetic properties

Laura Altenschmidt[1,a], Patricia Beaunier[2], Eric Riviére[1], Giulia Fornasieri[1], Amélie Bordage[1], and Anne Bleuzen[1,b]

[1] Institut de Chimie Moléculaire et des Matériaux d'Orsay, CNRS, Université Paris-Saclay, 91400 Orsay, France
[2] Sorbonne Université, CNRS, Laboratoire de Réactivité de Surface, LRS, 75005 Paris, France

Received 3 December 2021 / Accepted 9 April 2022 / Published online 29 April 2022

Abstract The magnetic properties of nanoparticle assemblies strongly depend on the structural and morphological characteristics of the individual nanoparticles as well as on their organization within the assembly. Here, we present the synthesis of cobalt and/or iron oxide nanoparticles within the ordered mesoporosity of a silica monolith by two different synthesis pathways (using either Prussian blue analogues or nitrate salts as a precursor). We describe the influence of the nature of the metal ion and of the synthesis pathway on the morphology of the nanoparticles. With respect to these observations, we present and discuss the temperature-dependent magnetic behaviors of the final nanocomposites.

1 Introduction

The use of nanoparticles in applications requires them to be transferred into macroscopic devices. A possible way to achieve this is the formation of nanoparticle assemblies in a macroscopic matrix, which allow to transfer the nanoscopic properties to the macroscale. Thereby, the final properties of the assembly depend on the properties of the individual nanoparticles, including the chemical composition, particle size and shape, and also on the spatial organization of these particles. Hence, it is necessary to well control all of these parameters simultaneously.

A possibility for such a high control that has been explored in the past years is the use of hard porous oxide templates. In a majority of cases, ordered silica templates are used. Thanks to the use of a surfactant-assisted sol–gel process it is possible to obtain calibrated pores and adjust the size and organization of the porosity [1,2]. However, these silica templates are typically obtained in powder form and thus do not present a macroscopic organization of the porosity. As a possible solution, the use of macroscopic ordered monoliths can be envisioned [3]. In that case, the sol–gel process and in particular the drying procedure have to be well controlled to ensure that the ordered silica network does not collapse and to avoid the formation of cracks [4,5]. Regardless of the silica morphology, the porosity has to be loaded with the precursor and for that purpose an impregnation with an aqueous solution containing metal salts is typically used. A thermal treatment in a controlled atmosphere results in the decomposition of the metal salts into oxides or alloys. By this technique, the formation of pure or doped Co_3O_4 [6,7], MnO_2 [8], maghemite or magnetite [9,10], CoFe [11] or FePt [12] particles has been reported among others. Besides the use of metal salts as the precursor, the coordination compound class of Prussian blue analogues (PBA) also received attention due to the fact that the metal ions are already perfectly mixed at the atomic scale. PBAs are made up of a cubic structure in which the metal ions are connected by cyanide bridges. As a result, the ratio between the metal ions can be well controlled in the resulting mixed metal oxides or alloys under the condition that it remains constant during the thermal decomposition. Such a high control over the chemical composition was shown by several studies using PBAs containing Mn, Fe, Co, Ni, Cu and Zn [13–18]. However, to synthesize PBAs in the mesoporosity, it is necessary to introduce the two reactants separately into the porosity of the silica template to ensure their reaction within the confined space. For example, one of the precursors can be introduced during the silica template formation [5] or the pores of the silica can be modified with anchoring groups [18–20].

[a] e-mail: laura.altenschmidt@universite-paris-saclay.fr (corresponding author)
[b] e-mail: anne.bleuzen@universite-paris-saclay.fr (corresponding author)

Studies of magnetic properties of nanoparticle assemblies embedded in silica matrices are already reported in the literature. The formation of chains consisting of metallic Co nanoparticles in the porosity of a SBA-15 powder leads to an increased coercive field with respect to the one of individual particles explained by the existence of interparticle coupling along the chains [21]. For the assembly of NiFe PBA nanoparticles within an ordered silica monolith, differences in the coercive field could be observed depending on the orientation of the pores in the applied magnetic field [3]. Another study looked at $CoFe_2O_4$ nanoparticles dispersed or not in a dense silica matrix [22]. The dispersion in silica leads to the formation of non-interacting superparamagnetic nanoparticles, whereas the non-embedded particles were strongly interacting. These studies show that even though the particle size, shape and chemical composition is well controlled, the variation of the organization of the particles can strongly influence the final magnetic properties of the nanoparticle assembly.
In this work, we present our approach of using the porosity of ordered mesoporous silica monoliths as a nanoreactor for the formation of Co and/or Fe oxide nanoparticles with a controlled size and morphology. Furthermore, we use PBAs to obtain a well-controlled chemical composition of the final nanoparticles and we compare these nanocomposites to those obtained by the use of nitrate salts, which are more frequently used in the literature. The influence of the nature of the metal ions and the synthesis pathway on the microstructure and on the magnetic properties of the nanoparticle assembly is discussed.

2 Experimental

The silica matrices were prepared using a bottom-up sol–gel approach. Here, we focused on systems containing Co and/or Fe ions. In a first step, the ordered mesoporous silica monoliths are synthesized. In a second step, two different synthesis pathways are used: the NO_3 synthesis pathway in which nitrate salts are used to load the pores, and the PBA synthesis pathway in which Prussian blue analogue nanoparticles are precipitated within the porosity. The final step consists of a thermal treatment in air to transform the precursors into oxide nanoparticles.

2.1 Synthesis of silica nanoreactor

In a first step, the hexagonally ordered mesoporous silica monolith was prepared; its synthesis is described in detail in another reference [23]. For a typical synthesis, 2.4 g of the co-polymer P123 were dissolved in 4 g tetramethyl orthosilicate (TMOS) at 50 °C. At room temperature 2 mL of acidified water (pH = 1.4; adjusted with HNO_3) were added and the solution stirred for 2 min and 30 s. At 23 °C, the sol was aged in a closed vial for 1 h and then for 1 week in air to give a monolith. The silica monolith was kept overnight at 80 °C and was calcined at 500 °C in air. These monoliths are denoted as ***Si-mono***. In addition, two other series of monoliths containing either 1 mol% Co^{2+} or Fe^{3+} ions were prepared. In these cases, 80 mg $Co(NO_3)_2 \cdot 6\ H_2O$ or 105 mg $Fe(NO_3)_3 \cdot 9\ H_2O$ were dissolved in the acidified aqueous solution prior to its addition. The remaining procedure remains unchanged. These monoliths are denoted as ***Co-mono*** and ***Fe-mono***, respectively.

2.2 Impregnation of monoliths and thermal treatment

A double solvent method was used to confine the aqueous impregnation solution within the porosity. The monoliths were immersed in heptane and the respective quantity of metal salt was dissolved in 1 ml distilled water.
For the PBA synthesis pathway, ***Co-mono*** was used as a nanoreactor for the formation of Prussian blue analogues, containing only Co or Co and Fe, whereas ***Fe-mono*** was used for the formation of Prussian blue. Prior to the addition of the hexacyanometallate solution (98.7 mg $K_3[Co(CN)_6]$ for CoCo PBA, 97.8 mg $K_3[Fe(CN)_6]$ for CoFe PBA, and 125.5 mg $K_4[Fe(CN)_6]$ for Prussian blue; corresponding to a ratio of 1:1 with respect to the Co^{2+} or Fe^{3+} ions already present in the silica matrix) 80 µl of HNO_3 (68%) were added. A volume equivalent to 80% of the porous volume of monolith was added to the monolith immersed in heptane. After 15 min, the impregnated monolith was washed 5 times with distilled water. The successful precipitation of the PBA nanoparticles was already done in previous studies [24], which showed that all of the Co ions are transformed into PBA during the impregnation and that they crystallize within the Fm3m space group.

For the NO_3 synthesis pathway, the ***Si-mono*** monolith was used as nanoreactor and the porosity loaded with nitrate salts, corresponding to 2 mol% (172.8 mg $Co(NO_3)_2$ for the pure Co system, 240.1 mg $Fe(NO_3)_3$ for the pure Fe system, and 86.5 mg $Co(NO_3)_2$ and 120.1 mg $Fe(NO_3)_3$ for the mixed system (molar ratio 1:1).
The thermal decomposition of the precursors was performed in air at 700 °C for 2 h with a ramp of 5 °C/min. The samples are denoted as ***XY Ox***, with X being the precursor (NO_3 or PBA) and Y being the nature of the element (Co and/or Fe). The Ox indicates the oxidative thermal decomposition of the precursors.

2.3 Instrumentation

For the characterization of the samples, the monoliths were finely ground. The powder X-ray diffraction pattern were collected on a Philips X'Pert diffractometer during 12 h with a step size of 0.033°. The transmission electron microscope images were collected on a JEOL JEM 2010 UHR microscope using a CCD camera (Gatan Orius Sc 1000). The particle sizes were determined using the ImageJ software and the value

of the standard deviation is given. For the magnetic measurements a Quantum Design MPMS XL7 magnetometer was used. The zero-field-cooled (ZFC) and field-cooled (FC) magnetization curves were measured with an applied magnetic field of 50 Oe and the magnetic field dependence of the magnetization was collected at 5 K. The magnetization values are given per gram of nanocomposite, unless stated otherwise.

3 Structural and morphological characterizations

The nanocomposites were characterized by powder X-ray diffraction (XRD) and transmission electron microscopy (TEM) to study the influence of the nature of the metal ions and of each synthesis pathway on the crystallinity and morphology of the nanoparticles. Moreover, the organization of the silica porosity and its influence on the organization of the nanoparticles is also analyzed by TEM.

3.1 X-ray diffraction

The diffraction patterns of ***NO3CoOx*** and ***PBACoOx***, ***NO3CoFeOx*** and ***PBACoFeOx***, and ***NO3FeOx*** and ***PBAFeOx*** are shown in Fig. 1a–c, respectively.

The diffraction peaks present a low intensity and are broadened regardless of the synthesis pathway and the nature of the metal ion. Nevertheless, it can be seen that the diffraction peaks appear to be more intense and better defined when the nanocomposites were obtained through the NO_3 synthesis pathway. Differences in the intensity of the diffraction peaks can also be observed with respect to the nature of the metal cation. Whereas, the diffraction peaks are well visible in the pure Co systems (Fig. 1a), for the nanocomposites containing only Fe the diffraction peaks are difficult to distinguish from the baseline, especially in the case of the ***PBAFeOx*** nanocomposite. The diffraction patterns of Co and Fe containing nanocomposites are intermediate between those of the pure Co and the pure Fe ones. These differences in the X-ray diffraction patterns suggest different behaviors of the Co and Fe ions: the former likely to form well crystallized nanoparticles and the latter leading to the formation of more disordered particles or particles with a smaller size. We would like to stress at this point that the analysis by XRD of very small particles embedded in a silica matrix can be challenging and a clear identification of the crystalline phase present in the composite cannot always unambiguously be done.

Despite the low intensity of the diffraction peaks, it is possible to index the visible peaks within a spinel oxide crystal system for the pure Co and CoFe systems. Figure 1a shows that both ***PBACoOx*** and ***NO3CoOx*** crystallize as Co_3O_4 and no other crystalline phases can be identified. In the case of ***PBACoFeOx*** and ***NO3CoFeOx*** (Fig. 1b), it can be seen that the position of the diffraction peaks of the nanocomposites is intermediate to the ones of the spinel oxides Co_3O_4 and $CoFe_2O_4$, suggesting either an intermediate chemical composition or the presence of several crystalline phases of $Co_{3-x}Fe_xO_4$ (x =0 - 3) with varying lattice parameters, such as Co_3O_4 and $CoFe_2O_4$. Indeed, in non-embedded PBA powder particles a demixing of the phases after a thermal treatment at 700 °C was observed [14]. Nonetheless, at the nanoscale the increased influence of the surface energy as well as the confinement in the silica matrix can lead to the stabilization of phases different from those observed in larger particles. Finally, in the case of the Fe only nanocomposites, the diffraction patterns of the nanocomposites are very close to the one of the pure silica matrix. It is not possible to obtain any information about the crystalline phase of the nanoparticles in ***PBAFeOx***, suggesting either a very small particle size or an amorphous character as mentioned above. Nevertheless, for the ***NO3FeOx*** sample, around the positions of the (311) and (440) diffraction lines of the maghemite phase, very broad and low-intense diffraction peaks can be seen. This suggests the possible formation of maghemite in the case of the NO_3 synthesis pathway. The formation of maghemite could be confirmed thanks to an analysis by Fe K-edge X-ray absorption spectroscopy on the SAMBA beamline at SOLEIL (Fig. 7). The XANES spectrum of ***NO3FeOx*** exhibits the same spectral features as the one of maghemite, whereas it is clearly different from the hematite one. This indicates the formation of maghemite rather than hematite in ***NO3FeOx***. The formation of maghemite, despite not being the thermodynamically stable Fe_2O_3 polymorph, has already been reported in $Fe_2O_3-SiO_2$ nanocomposites prepared by a sol–gel method [25]. Cannas et al. [25] thus showed that at a thermal treatment above 700 °C maghemite is mainly formed in the silica nanocomposites with a sufficiently low Fe^{3+} ions concentration. This can be understood by an effect of the particle size and the increased influence of the surface energy responsible for the stabilization of iron oxide phases, different from the thermodynamically most stable one [26].

3.2 Transmission electron microscopy

The TEM and HR-TEM data for each metal ion system are presented in Figs. 2, 3 and 4, respectively, and are discussed with respect to the nature of the metal ions as well as the synthesis pathway. In all cases the hexagonally organized mesoporosity of the silica matrix is still visible and thus withstands the thermal treatment at 700 °C. It can be seen that some pores are filled with dark spots which are attributed to the oxide nanoparticles.

The data for the pure Co system is shown in Fig. 2. It can be seen that the shape of the nanoparticles strongly depends on the synthesis pathway. Whereas the nanoparticles in ***PBACoOx*** are spherical, in the case of ***NO3CoOx*** the formation of nanorods can be observed. The diameter of these particles is 3.9 ±

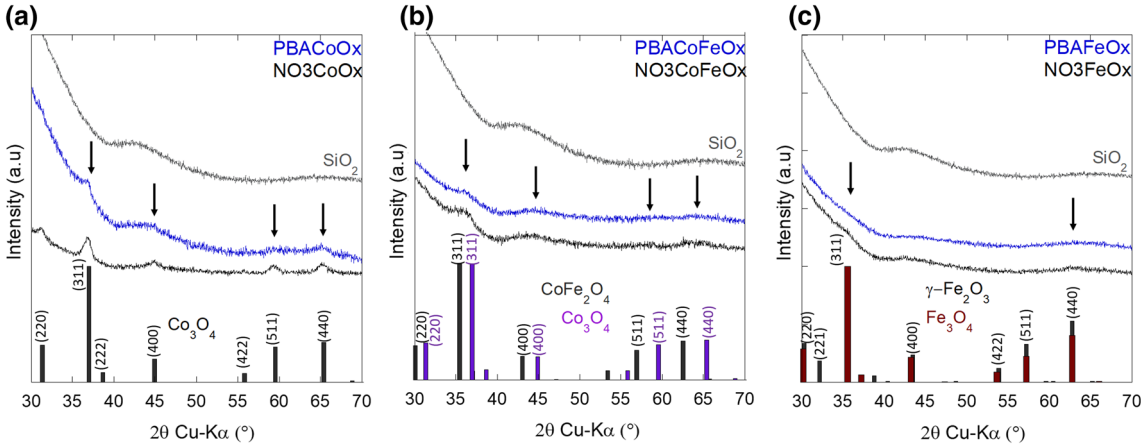

Fig. 1 Powder X-ray diffraction patterns of the nanocomposites and the expected diffraction lines of the corresponding spinel oxides: **a** ***NO3CoOx*** and ***PBACoOx*** compared to the diffraction lines of Co_3O_4, **b** ***NO3CoFeOx*** and ***PBACoFeOx*** compared to the diffraction line of Co_3O_4 and $CoFe_2O_4$, and **c** ***NO3FeOx*** and ***PBAFeOx*** compared to the diffraction lines of $\gamma - Fe_2O_3$ and Fe_3O_4. The arrows indicate the position of the diffraction peaks. The diffraction pattern of the pure silica matrix is presented in each figure for comparison. The broad peak at 43° 2θ arises from the sample holder

0.6 nm for ***PBACoOx*** (Fig. 2b) and 4.7 ± 0.6 nm for ***NO3CoOx*** (Fig. 2e) with a narrow size distribution. These diameters are in good agreement with the pore diameter of the silica pores (5–6 nm, determined by N_2 physisorption measurements [5]), showing the confinement effect of the matrix on the particle growth. Regarding the length of the nanorods present in ***NO3CoOx*** particles up to 49 nm can be found. This difference in particle sizes is in agreement with the width of the diffraction peaks (Fig. 1a), which are significantly narrower in the case of ***NO3CoOx***, made of larger size particles. Regardless of the synthesis pathway, the formation of monocrystalline particles is evidenced by HRTEM (Fig. 2c and f) and the inter-reticular distances can be assigned to the lattice planes of Co_3O_4. This confirms the results obtained by XRD.

The TEM data for the Fe only system are presented in Fig. 3. The dark spots unambiguously reveal the presence of oxide nanoparticles in the matrix porosity (Fig. 3a and d). The diameters of the particles are 4.3±0.7 nm for ***NO3FeOx*** (Fig. 3e) and 4.1±1.0 nm for ***PBAFeOx*** (Fig. 3b); these values are again in agreement with the diameter of the silica pores, indicating a confinement effect of the porous matrix on the particles growth. For ***NO3FeOx***, the representative HR-TEM image (Fig. 3f) shows that the nanoparticles are monocrystalline and Fig. 3d indicates that they form nanorods, as in the case of ***NO3CoOx***, or that they are aggregated or in close proximity to one another along the silica pores. The inter-reticular distance of 2.48 Å cannot unambiguously be assigned to a certain iron oxide phase since this lattice plane distance occurs in maghemite as well as in hematite. Therefore, the TEM analysis only allows to confirm the presence of crystalline nanoparticles as suggested by XRD (Fig. 1c). In the case of ***PBAFeOx***, it was not possible to obtain a HR-TEM image showing crystalline nanoparticles, which suggests the formation of amorphous or low-crystalline nanoparticles, which is in agreement with the absence of diffraction peaks (Fig. 1c).

At last, the data for the CoFe systems are shown in Fig. 4. Both synthesis pathways lead to a narrow particle size distribution with particle diameters of 3.5 ± 0.7 nm for ***PBACoFeOx*** (Fig. 4b) and 4.3 ± 0.7 nm for ***NO3CoFeOx*** (Fig. 4e). In the case of ***PBACoFeOx***, the particles are monocrystalline as evidenced by the appearance of inter-reticular planes on the representative HRTEM image (Fig. 4c) and lattice plane distances close to the ones found in Co_3O_4 and $CoFe_2O_4$ can be measured. In contrast, the particles in ***NO3CoFeOx*** present various lengths and polycrystalline (Fig. 8) as well as monocrystalline (Fig. 4f) particles can be identified. The simultaneous presence of mono- and polycrystalline particles suggests that individual particles fuse together during the thermal treatment. Furthermore, in ***NO3CoFeOx***, we could also observe a significant variation of the Co/Fe ratio from one analyzed region to another by an EDS analysis (Fig. 9a). This indicates a phase separation and the formation of Co- and Fe-rich particles. We propose to explain this chemical heterogeneity in ***NO3CoFeOx*** as a result of (i) the diffusion of the ions in solution and phase separation occurring during the crystallization of the nitrate salts within the pores after impregnation and/or, (ii) of the diffusion of the ions in the molten nitrate salts during the thermal treatment and phase separation occurring during the oxide phase formation. In contrast, in ***PBA-CoFeOx***, the EDS analysis indicates a Co/Fe ratio of 1.5 in the different regions without significant variations (Fig. 9b), in agreement with the Co/Fe ratio in the initial CoFe PBA $Co_4[Fe(CN)_6)_{2.7}$, suggesting that the chemical composition in the PBA precursor is maintained in the oxide nanoparticles. The homogeneity in ***PBACoFeOx*** can be explained by the rapid PBA pre-

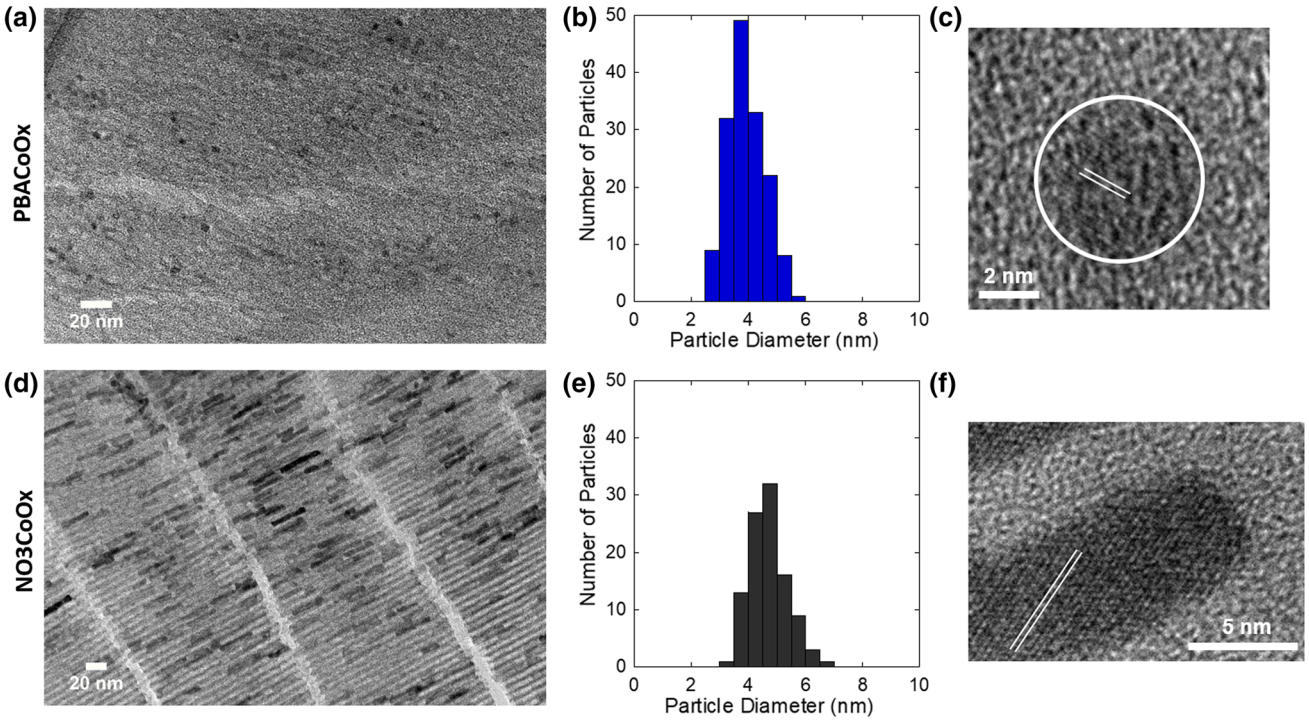

Fig. 2 Representative TEM images of **a** ***PBACoOx*** and **d** ***NO3CoOx***; particle diameter distributions for **b** ***PBACoOx*** and **e** ***NO3CoOx***; HR-TEM images of **c** ***PBACoOx*** and **f** ***NO3CoOx***

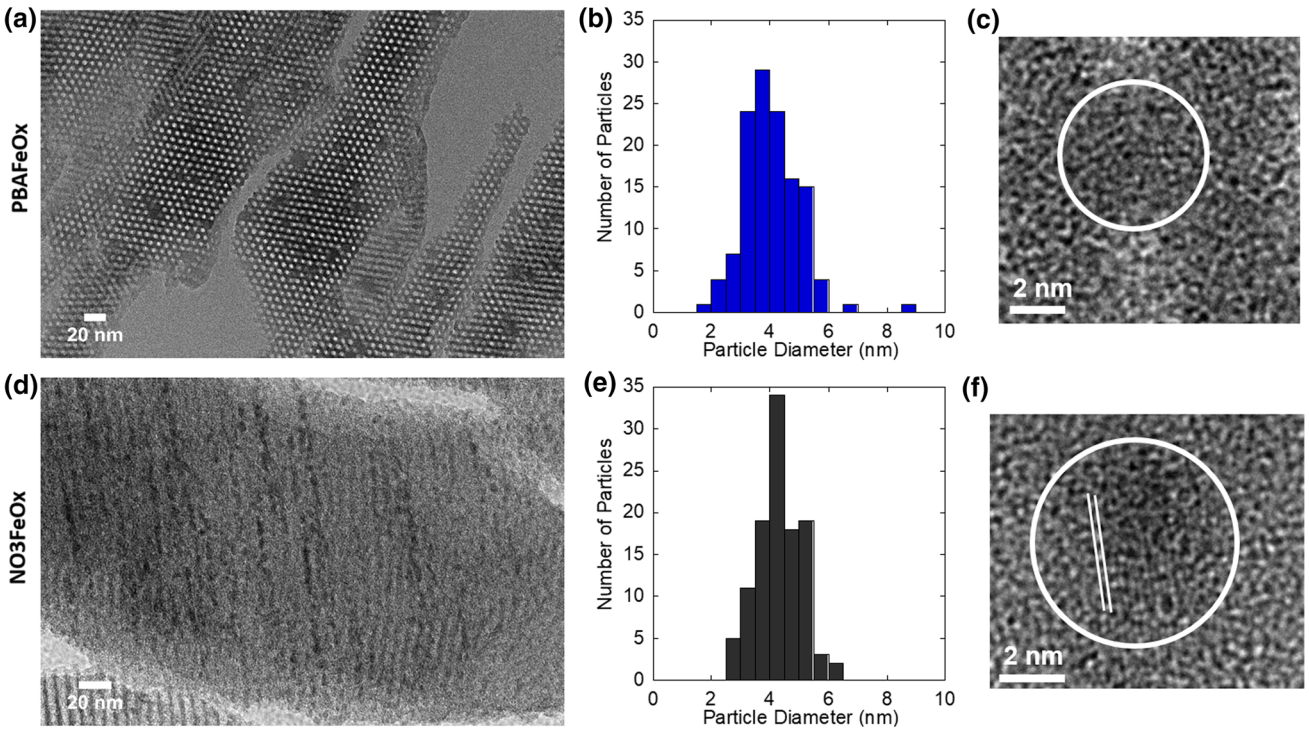

Fig. 3 Representative TEM images of **a** ***PBAFeOx*** and **d** ***NO3FeOx***; particle diameter distributions for **b** ***PBAFeOx*** and **e** ***NO3FeOx***; HR-TEM images of **c** ***PBAFeOx*** and **f** ***NO3FeOx***

cipitation and the solid-solid PBA-oxide transformation preventing the diffusion of the ions and a phase separation.

By comparing the results obtained for the nanocomposites resulting from the two synthesis pathways, we can conclude that the choice of the synthesis pathway has a significant influence on the final nano- and microstructure of the oxide nanoparticles.

Regarding the chemical composition and the structure of the nanoparticles, for the cobalt-based nanocomposites, the only phase formed is unsurprisingly the thermodynamically stable Co_3O_4 phase, regardless of the synthesis pathway.

In the case of the Fe-based nanocomposites, the main point regarding the oxide phase formed is the overall low degree of crystallinity, which might be due to the polymorphism of iron(III) oxides, which can crystallize in the α, β, γ and ε phases among others. The formation of crystalline maghemite particles in a silica matrix from nitrate salts as precursors after a thermal treatment at 700 °C was already observed [25]. This is in agreement with our observations. Given the comparable particle size for both synthesis pathways (4.3 versus 4.1 nm) and exactly the same treatment applied to the nanocomposites, the lower crystallinity of the oxide particles obtained via the PBA synthesis pathway can have two origins: (i) the difference in local atmosphere produced by the decomposition of the NO_3^- or CN^- counter-ions and/or (ii) the higher local concentration of precursors (higher aggregation state) via the NO_3 synthesis pathway than via the PBA one, leading to a local overheat accompanying the exothermic transformation, higher for the NO_3 synthesis pathway than for the PBA one. The latter proposition is in line with the predominantly amorphous particles obtained in reference [25] for thermal treatment temperatures less than 700°C.

At last, in the CoFe-based nanocomposites containing oxide nanoparticles having a size comparable to those formed in the Co and Fe nanocomposites, the degree of crystallinity is comparable to that of the Co-based systems and can, therefore, be associated with the presence of the Co species. The main difference between the NO_3 and the PBA synthesis pathway is the distribution of the Co and Fe species within the oxide particles. Homogeneously mixed in the PBA precursors, the Co/Fe ratio is maintained in all oxide particles formed. In contrast, phase segregation probably occurs as soon as a solid phase appears from the mixture of nitrate salts. The presence of a wide range of nanoparticles with various Co/Fe ratios and therefore different cell parameters, in addition to the small particle size, fully explains the broad XRD peaks for ***NO3CoFeOx*** in Fig. 1.

Regardless of the nature of the metal ion, the particle diameters present a narrow size distribution and are also in good agreement with the pore diameter of the silica matrix, thus resulting from a good confinement effect of the matrix on the particle growth. However, when using the NO_3 synthesis pathway, the particle diameter is slightly increased in comparison to that of the particles formed in the nanocomposites obtained through the PBA synthesis pathway. This can be explained by the different nature of the precursor. In the PBA synthesis pathway, spherical PBA nanoparticles are rapidly formed as soon as both reactive precursors, homogeneously distributed in the pores, come into contact. During the thermal treatment of the PBA nanoparticles, the cyanide bridges are replaced by oxo-bridges leading to a densification and shrinkage of the nanoparticles, resulting in a diameter slightly smaller than the diameter of the pores. In contrast, in the case of nitrate salts it can be assumed that the precursors remain in solution or precipitate in the porosity after impregnation. During the thermal treatment, the nitrate salts, still in solution or resolubilized, are able to diffuse so that the oxide particles can expand up to the walls of the silica matrix, leading to an increased oxide particle diameter.

Concerning the main morphological differences, it could be shown that in the case of the NO_3 synthesis pathway the formation of elongated or aggregated particles along the pore channels can be observed which can be assigned to the shape or aggregation state of the initial particles formed by the nitrate salts after impregnation or during the thermal treatment. In contrast, the PBA synthesis pathway leads to stable, spherical PBA nanoparticles homogeneously distributed along the cylindrical pores of the matrix, resulting in spherical oxide nanoparticles with a size below the diameter of the silica pores after thermal treatment. This shows that by changing the precursor, it is possible to directly influence the morphology and/or the distribution of the spinel oxide nanoparticles.

Therefore, thanks to the use of a silica matrix, which is restricting the growth of the particles, a high control over the particle size and its distribution can be achieved. Due to this confinement effect, it is possible to synthesize comparable nanoparticle assemblies which mainly differ in the chemical composition of the nanoparticles.

4 Magnetic properties

From the literature, different magnetic behaviors are expected for the three systems due to the different natures of the metal ions present within the nanoparticles. For Co_3O_4, an antiferromagnetic behavior with a Neel temperature of 33 K is reported, as well as a shift of the irreversibility temperature between the zero-field-cooled (ZFC) and the field-cooled (FC) magnetization curves to lower temperatures with decreasing particle size [27,28]. Maghemite exhibits a ferrimagnetic behavior in bulk form with a high Curie temperature of 928 K [29], but in nanoparticles, the magnetic blocking temperature depends on the nanoparticles size and interparticle interactions [30]. Therefore, for the mixed CoFe systems, depending on the chemical composition and the ratio between the Co and Fe ions, the magnetic

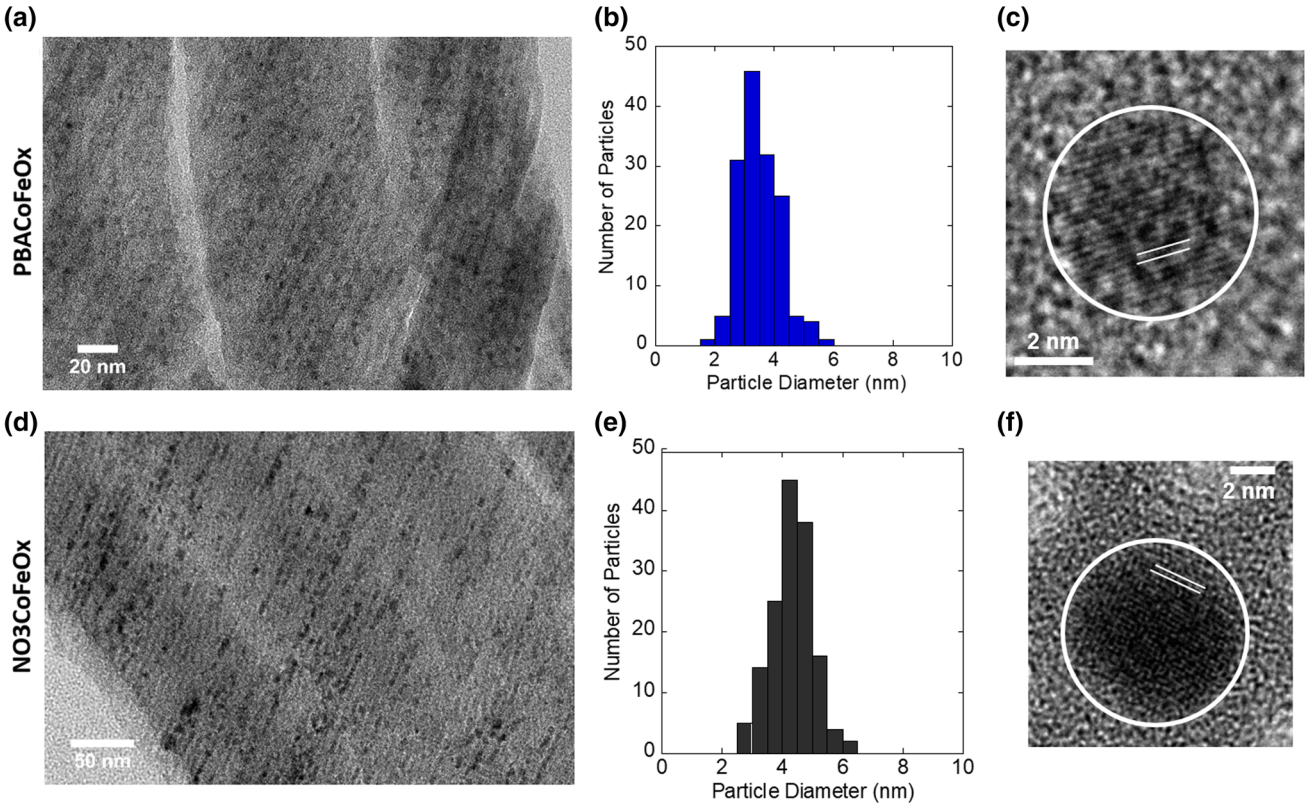

Fig. 4 Representative TEM images of **a** ***PBACoFeOx*** and **d** ***NO3CoFeOx***; particle diameter distributions for **b** ***PBACoFeOx*** and **e** ***NO3CoFeOx***; HR-TEM images of **c** ***PBACoFeOx*** and **f** ***NO3CoFeOx***

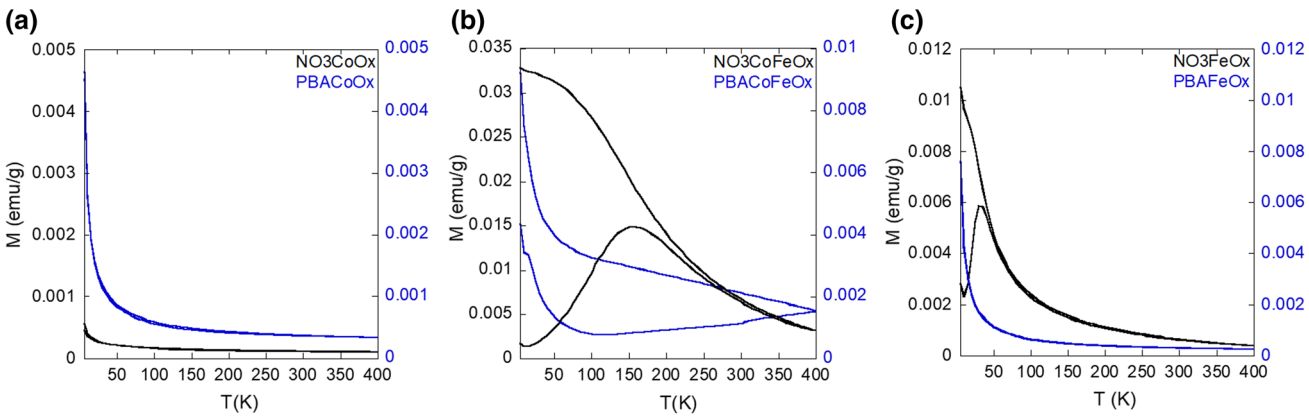

Fig. 5 ZFC–FC magnetization curves of the nanocomposites **a** ***NO3CoOx*** and ***PBACoOx***, **b** ***NO3CoFeOx*** and ***PBACoFeOx***, and **c** ***NO3FeOx*** and ***PBAFeOx***. The left y-axis corresponds to the NO_3 synthesis pathway and the right one to the PBA synthesis pathway

behavior should vary between antiferromagnetism and ferrimagnetism depending on the Co/Fe ratio, modified by nanoscale effects.

For all nanocomposites, the ZFC–FC magnetization curves were measured in the 5–400 K temperature range. They are shown in Fig. 5a–c for the Co-based systems, the CoFe-based systems and the Fe-based systems, respectively.

The shape of the magnetization curves of the Co only nanocomposites (Fig. 5a) is comparable. Mainly their intensity varies. A further analysis by a reproduction of the magnetic susceptibility of ***NO3CoOx*** over the paramagnetic temperature range with a Curie–Weiss law is in agreement with an antiferromagnetic behavior of the compound. In contrast, ***PBACoOx*** rather presents a pure paramagnetic behavior. The significantly higher magnetization value in ***PBACoOx***

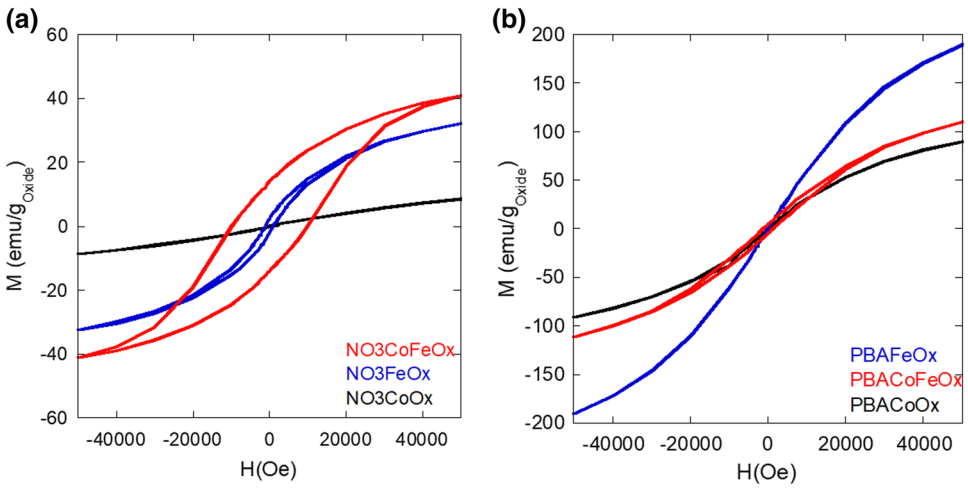

Fig. 6 Magnetic field dependence of the magnetization measured at 5 K of **a** ***NO3CoOx***, ***NO3FeOx***, ***NO3CoFeOx*** and **b** ***PBACoOx***, ***PBAFeOx***, ***PBACoFeOx***

than in ***NO3CoOx*** over the whole temperature range reflects a Co^{II}/Co^{III} ratio higher in ***PBACoOx*** than in ***NO3CoOx***. The differences in the morphology of the nanoparticles are able to qualitatively explain these different behaviors. The surface–to-volume ratio of the nanoparticles is different in ***PBACoOx*** and in ***NO3CoOx***. A Co^{II}/Co^{III} ratio different at the surface and in the core of the nanoparticles, such as a higher Co^{II}/Co^{III} ratio at the surface, could explain the higher magnetization of ***PBACoOx***. Furthermore, since the nanoparticles are significantly smaller and significantly more distant in ***PBACoOx*** than in ***NO3CoOx***, it could be possible that they are too small and do not contain a sufficient quantity of unit cells or the interparticle interactions are not strong enough to show a collective behavior in the studied temperature range.

In the case of the Fe only nanocomposites (Fig. 5c), ***PBAFeOx*** presents a paramagnetic behavior, whereas the ZFC magnetization curve of ***NO3FeOx*** presents a maximum around 33 K. We were able to assign this magnetic feature to a pure superparamagnetic behavior by measuring the frequency-dependent AC magnetic susceptibility (Fig. 10) and by fitting the relaxation time with an Arrhenius law ($\tau_0 = 6.9 \cdot 10^{-12}$ s; $Ea/k_B = 912.3$ K). Such a behavior has already been reported in the literature for maghemite nanoparticles of comparable size [30,31]. Again, these differences in the magnetic behavior can be qualitatively explained by the differences in the microstructure of the nanocomposites. The particles in ***PBAFeOx*** are most likely amorphous and present a smaller particle size, hence resulting in an overall paramagnetic behavior.

Therefore, the Co only and Fe only nanocomposites prepared via the NO_3 synthesis pathway present a magnetic behavior in agreement with that of comparable systems reported in the literature. It can however be noticed that the Co only and Fe only nanocomposites prepared via the PBA synthesis pathway do not find directly comparable systems in the literature and a further size or interparticle interactions reduction is needed to explain the properties.

When we now consider the intermediate system containing both Co and Fe ions (Fig. 5b), it can be seen that the magnetization curves are complex. The ZFC magnetization curve of ***NO3CoFeOx*** presents a maximum centered around 155 K, which is strongly broadened over the entire temperature range, suggesting a wide contribution of energy barriers. For a further interpretation of the ZFC maximum, a frequency-dependent AC magnetic susceptibility measurement was performed (Fig. 11a). The temperature dependence of the relaxation time could be reproduced by a Power law ($\tau = \tau_0 \cdot (T_g/(T - T_g)^{z\nu}$ with $T_g = 126$ K, $\tau_0 = 1.16 \cdot 10^{-6}$ s, $z\nu = 13.7$) revealing a spin-glass like behavior in ***NO3CoFeOx***. This spin-glass like magnetic behavior can be related to the heterogeneous chemical composition of the nanoparticles caused by a phase separation. Moreover, an exchange bias effect can be evidenced in ***NO3CoFeOx*** (Fig. 12a). This confirms the demixing and the formation of antiferromagnetic Co-rich particles and ferrimagnetic Fe-rich phases in close proximity, in agreement with the XRD and TEM results. In the case of ***PBACoFeOx***, the maximum of the ZFC magnetization curve is shifted above 400 K and the peak is even more broadened. However, this is rather surprising considering the more homogeneous morphology of these particles. Additionally, at low temperatures, a paramagnetic contribution can be evidenced in ***PBACoFeOx*** which is not present in ***NO3CoFeOx***. Furthermore, no exchange bias effect can be evidenced in ***PBACoFeOx*** (Fig. 12b). For the further characterization of the magnetic behavior of ***PBACoFeOx***, we performed AC magnetic measurements (Fig. 11b). No frequency dependence could be evidenced neither for the in-phase nor the out-of-phase component, showing the presence of a collective behavior resulting in a blocking of the magnetic moments even at elevated temperatures. We propose to explain the shift of the temperature maximum in the ZFC curve by the different sizes of the particles, resulting in dif-

ferent magnetic moments per particles and different strengths of interparticle interactions [32].

The magnetic properties of the nanocomposites were further investigated by the measurement of the magnetic field dependence of the magnetization at 5 K. The magnetization curves are shown in Fig. 6a for ***NO3CoOx***, ***NO3FeOx***, ***NO3CoFeOx*** and in Fig. 6b for ***PBACoOx***, ***PBAFeOx***, ***PBACoFeOx***. The magnetization is given per gram of Co and/or Fe oxide present in the nanocomposite.

Due to the unknown exact chemical composition of the nanocomposites and the unknown exact mass of the expected oxide in the analyzed sample, only the order of magnitude of the saturation magnetization values will be discussed on the basis that a few emu/g are expected for nanoscale antiferromagnets such as Co_3O_4 or $\alpha - Fe_2O_3$ while a few tens of emu/g are expected for nanoscale ferrimagnets like $\gamma - Fe_2O_3$ or $CoFe_2O_4$. The saturation magnetization value of 9 emu/g and the shape of the curve of ***NO3CoOx*** is in line with the presence of a nanoscale antiferromagnet such as Co_3O_4 in agreement with all other characterizations. The saturation magnetization value of 41 emu/g and the large coercive field (9830 Oe) of ***NO3CoFeOx*** is the signature of the presence of a nanoscale ferrimagnet with an important magnetic anisotropy, in line with the presence of the Fe rich $CoFe_2O_4$ oxide phase in the nanocomposite and the phase separation proposed above. At last, the saturation magnetization value of 32 emu/g and the shape of the curve of ***NO3FeOx*** is in line with the presence of a nanoscale ferrimagnet, which again confirm the presence of the maghemite phase in this nanocomposite.

In contrast, the nanocomposites obtained by the PBA synthesis pathway (Fig. 6b) exhibit completely different magnetic behaviors. Neither ***PBACoOx*** nor ***PBAFeOx*** present an opening of the hysteresis cycle. The shape of the curve resembles the one expected for a paramagnetic compound, which reminds the significant paramagnetic contribution also detected in the ZFC–FC magnetization curves (Fig. 5a and c). The curve of ***PBACoFeOx*** exhibits a hysteresis cycle with a coercive field of 1230 Oe, indicating the presence of a ferrimagnetic phase. However, the significant difference between the magnetization curves of ***NO3CoFeOx*** and ***PBACoFeOx*** suggests the formation of a different magnetic phase other than $CoFe_2O_4$ in the latter. This different phase can correspond to a CoFe mixed oxide with a Co/Fe ratio of 1.5, as suggested by the TEM and EDS analyses.

In the series of the studied systems, the magnetic behavior of the CoFe system is surprising. In the pure Co and the pure Fe systems, a collective magnetic behavior is always observed in the sample resulting from the NO_3 synthesis pathway whereas the systems resulting from the PBA synthesis pathway exhibit no collective behavior. This can be explained by different size and crystallinity of the particles as well as different interparticle distances. The situation is different for the CoFe systems. In that case, the two samples resulting from the different synthesis pathways both exhibit a collective magnetic behavior, but the temperature of the ZFC curve maximum corresponding to the blocking or the freezing temperature, is significantly higher in the case of ***PBACoFeOx***. Despite being the intermediate system, the magnetic behavior cannot be described as intermediate between the two extreme systems. The simultaneous presence of cobalt and iron in the particles can lead to (i) an increased magnetic moment borne by each particle and (ii) an enhancement of the magnetic anisotropy induced by the presence of the Co^{II} ions, which can explain an overall strengthening of the collective magnetic behavior. The significant different magnetic behaviors of the two systems can stem from several parameters: (i) different homogeneity of the nanoparticles chemical composition, different particle size and organization in the solid matrix.

5 Conclusion

In this study, we were able to show that the choice of the precursor for the formation of oxide nanoparticle assemblies is crucial and can be used to selectively control the morphology and/or the organization of the nanoparticles. The use of nitrate salts as precursor leads to the formation of elongated or aggregated particles, whereas PBAs result in only spherical nanoparticles and more homogeneously distributed within the silica matrix. As a result of these differences, the magnetic behavior of the nanoparticle assemblies is strongly affected. The spherical particles derived from the PBA synthesis pathway always present a significant paramagnetic contribution, that we are not able to fully explain within the frame of this study. In the case of the ***PBACoFeOx*** nanocomposite, the presence of strong interparticle interactions can also be evidenced. On the other hand, the NO_3 synthesis pathway leads to the expected magnetic behavior of an antiferromagnetic (***NO3CoOx***) or superparamagnetic (***NO3FeOx***) nanoparticle assembly. Due to the complex chemical composition of ***NO3CoFeOx***, the magnetic behavior of the assembly is also more complex.

Our approach can be used for the synthesis of nanoparticle assemblies which are comparable to one another. This allows to selectively study and understand the influence of distinct synthesis parameters on the final magnetic properties.

Acknowledgements This research was supported by Paris-Saclay University and the CNRS. L.A. thanks the French government for the PhD financial support. The authors acknowledge SOLEIL for the provision of synchrotron radiation facility on the SAMBA beamline through proposal 20180973.

Appendix: Supporting figures

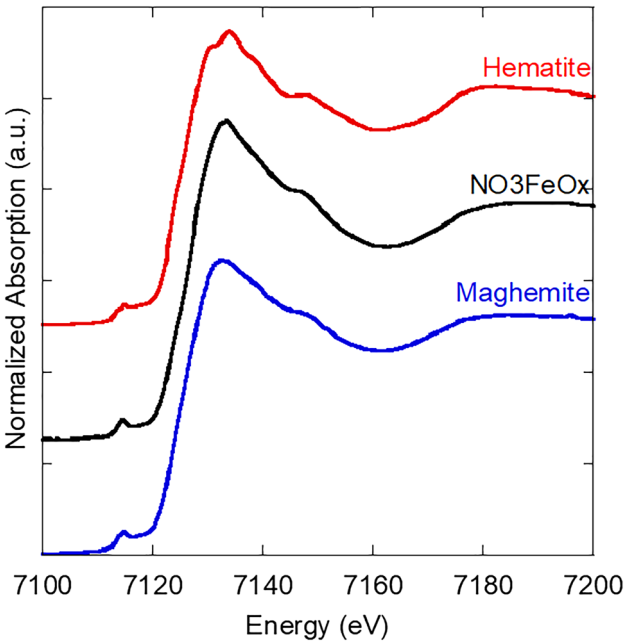

Fig. 7 Normalized Fe K-edge XANES spectra of ***NO3FeOx*** compared with the spectra of the maghemite and hematite references. It can be seen that the spectrum of ***NO3FeOx*** exhibits the same spectral features as the one of maghemite, whereas it is clearly different from the hematite one. This indicates the formation of maghemite rather than hematite in ***NO3FeOx***. The spectra were measured in transmission mode on the SAMBA beamline at SOLEIL (Gif-sur-Yvette, France). They were conventionally normalized using the ATHENA software and energy calibrated after measurement. The acquisition was performed at room temperature in a continuous mode from 6900 to 8300 eV. No radiation damage was observed. The references were measured as pellets diluted in BN and ***NO3FeOx*** was placed between two pieces of kapton tape

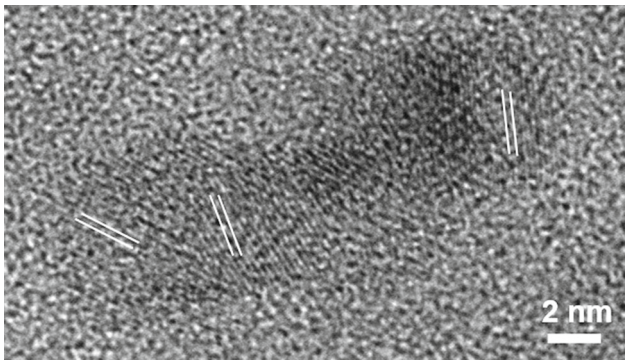

Fig. 8 HR-TEM image of ***NO3CoFeOx*** showing a polycrystalline nanorod

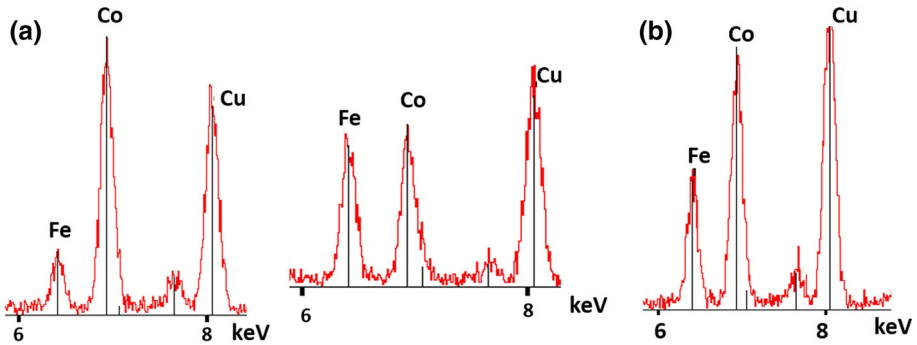

Fig. 9 Representative EDS spectra of **a** ***NO3CoFeOx*** showing the strong variations of the Co/Fe ratio within the different regions of the nanoparticle assembly, and **b** ***PBACoFeOx*** showing a Co/Fe ratio of 1.5

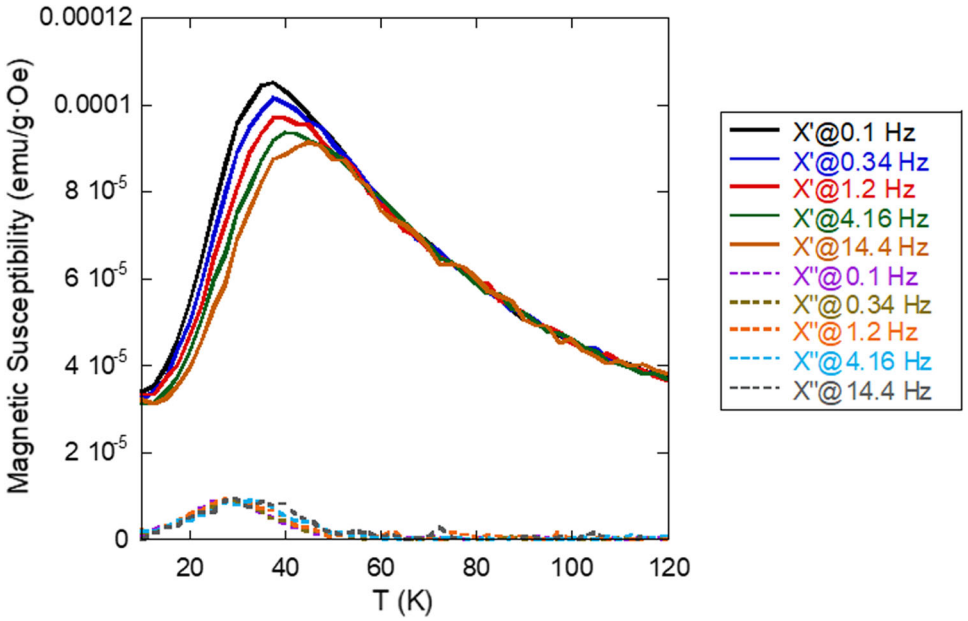

Fig. 10
Frequency-dependent AC magnetic measurements of ***NO3FeOx*** in the 10–120 K temperature range

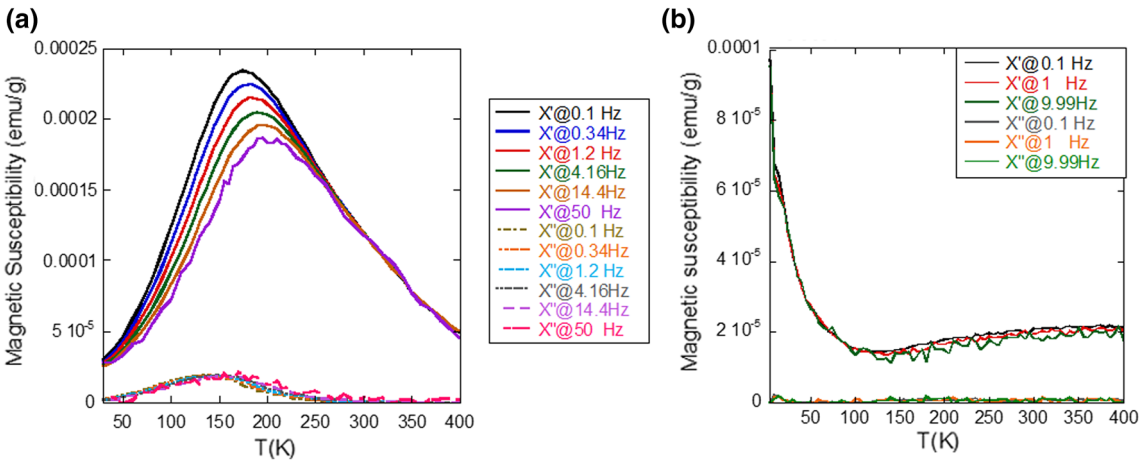

Fig. 11 In-phase (χ') and out-of-phase (χ") components of the AC magnetic susceptibility as a function of temperature of **a** ***NO3CoFeOx*** and **b** ***PBACoFeOx***

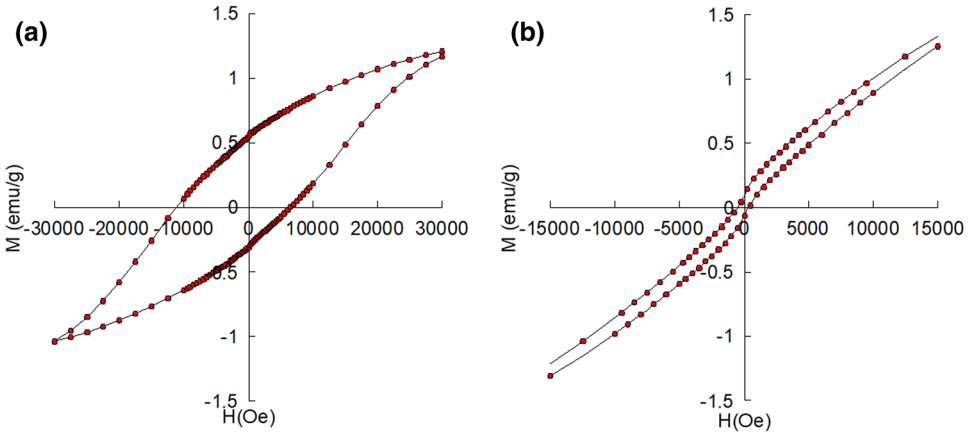

Fig. 12 Magnetization measured at 5 K after cooling from 300 K with an applied field of H = 30 kOe of **a** ***NO3CoFeOx*** and **b** ***PBACoFeOx***

References

1. D. Zhao, J. Feng, Q. Huo, N. Melosh, G.H. Fredrickson, B.F. Chmelka, G.D. Stucky, Science **279**, 548–552 (1998)
2. J.S. Beck, J.C. Vartuli, W.J. Roth, M.E. Leonowicz, C.T. Kresge, K.D. Schmitt, C.T.W. Chu, D.H. Olson, E.W. Sheppard, S.B. McCullen, J.B. Higgins, J.L. Schlenker, J. Am. Chem. Soc. **114**, 10834–10843 (1992)
3. R. Moulin, G. Fornasieri, M. Impéror-Clerc, E. Rivière, P. Beaunier, A. Bleuzen, ChemNanoMat **3**, 833–840 (2017)
4. H. Yang, Q. Shi, B. Tian, S. Xie, F. Zhang, Y. Yan, B. Tu, D. Zhao, Chem. Mater. **15**, 536–541 (2003)
5. P. Durand, G. Fornasieri, C. Baumier, P. Beaunier, D. Durand, E. Rivière, A. Bleuzen, J. Mater. Chem. **20**, 9348–9354 (2010)
6. E.L. Salabas, A. Rumplecker, F. Kleitz, F. Radu, F. Schuth, Nano Lett. **6**, 2977–2981 (2006)
7. J. Rosen, G.S. Hutchings, F. Jiao, J. Catal. **310**, 2–9 (2014)
8. M. Imperor-Clerc, D. Bazin, M.-D. Appay, P. Beaunier, A. Davidson, Chem. Mater. **16**, 1813–1821 (2004)
9. E. Delahaye, V. Escax, N.E. Hassan, A. Davidson, R. Aquino, V. Dupuis, R. Perzynski, Y.L. Raikher, J. Phys. Chem. B **110**, 26001–26011 (2006)
10. V. Matsura, Y. Guari, J. Larionova, C. Guérin, A. Caneschi, C. Sangregorio, E. Lancelle-Beltran, A. Mehdi, R.J.P. Corriu, J. Mater. Chem. **14**, 3026–3033 (2004)
11. D. Carta, G. Mountjoy, R. Apps, A. Corrias, J. Phys. Chem. C **116**, 12353–12365 (2012)
12. E. Kockrick, P. Krawiec, W. Schnelle, D. Geiger, F.M. Schappacher, R. Pöttgen, S. Kaskel, Adv. Mater. **19**, 3021–3026 (2007)
13. Y. Guo, R. Weiss, M. Epple, Eur. J. Inorg. Chem. **2005**, 3072–3079 (2005)
14. V. Trannoy, A. Bordage, J. Dezalay, R. Saint-Martin, E. Rivière, P. Beaunier, C. Baumier, C. La Fontaine, G. Fornasieri, A. Bleuzen, CrystEngComm **21**, 3634–3643 (2019)
15. D. Liu, R. Qiang, Y. Du, Y. Wang, C. Tian, X. Han, J. Colloid Interface Sci. **514**, 10–20 (2018)
16. X. Hou, G. Zhu, X. Niu, Z. Dai, Z. Yin, Q. Dong, Y. Zhang, X. Dong, J. Alloys Compd. **729**, 518–525 (2017)
17. M. Cheng, Y. Liu, D. Huang, C. Lai, G. Zeng, J. Huang, Z. Liu, C. Zhang, C. Zhou, L. Qin, W. Xiong, H. Yi, Y. Yang, Chem. Eng. J. **362**, 865–876 (2019)
18. B. Folch, J. Larionova, Y. Guari, L. Datas, C. Guérin, J. Mater. Chem. **16**, 4435–4442 (2006)
19. B. Folch, Y. Guari, J. Larionova, C. Luna, C. Sangregorio, C. Innocenti, A. Caneschi, C. Guérin, New J. Chem. **32**, 273–282 (2008)
20. G. Clavel, Y. Guari, J. Larionova, C. Guérin, New J. Chem. **29**, 275–279 (2005)
21. A.F. Gross, M.R. Diehl, K.C. Beverly, E.K. Richman, S.H. Tolbert, J. Phys. Chem. B **107**, 5475–5482 (2003)
22. D. Peddis, C. Cannas, A. Musinu, G. Piccaluga, Chem. Eur. J. **15**, 7822–7829 (2009)
23. E. Delahaye, R. Moulin, M. Aouadi, V. Trannoy, P. Beaunier, G. Fornasieri, A. Bleuzen, Chem. Eur. J. **21**, 16906–16916 (2015)
24. M. Aouadi, G. Fornasieri, V. Briois, P. Durand, A. Bleuzen, Chem. Eur. J. **18**, 2617–2623 (2012)
25. C. Cannas, D. Gatteschi, A. Musinu, G. Piccaluga, C. Sangregorio, J. Phys. Chem. B **102**, 7721–7726 (1998)
26. M. Popovici, M. Gich, D. Niznansky, A. Roig, C. Savii, L. Casas, E. Molins, K. Zaveta, C. Enanche, J. Sort, Sd. Brion, G. Chouteau, J. Nogués, Chem. Mater. **16**, 5542–5548 (2004)
27. Y. Ichiyanagi, Y. Kimishima, S. Yamada, J. Magn. Magn. Mater. **272–276**, E1245–E1246 (2004)
28. Y. Ichiyanagi, S. Yamada, Polyhedron **24**, 2813–2816 (2005)
29. S. Sakurai, A. Namai, K. Hashimoto, S.-I. Ohkoshi, J. Am. Chem. Soc. **131**, 18299–18303 (2009)
30. K. Nadeem, H. Krenn, T. Traussnig, R. Würschum, D.V. Szabó, I. Letofsky-Papst, J. Magn. Magn. Mater. **323**, 1998–2004 (2011)
31. L.A. Mercante, W.W.M. Melo, M. Granada, H.E. Troiani, W.A.A. Macedo, J.D. Ardison, M.G.F. Vaz, M.A. Novak, J. Magn. Magn. Mater. **324**, 3029–3033 (2012)
32. G. Muscas, G. Concas, S. Laureti, A.M. Testa, R. Mathieu, J.A. De Toro, C. Cannas, A. Musinu, M.A. Novak, C. Sangregorio, S.S. Lee, D. Peddis, Phys. Chem. Chem. Phys. **20**, 28634–28643 (2018)